



# Temperature and external strain sensing with metal-embedded optical fiber sensors for structural health monitoring

QIANG BIAN,<sup>1,2,\*</sup>  ALEXANDER PODHRAZSKY,<sup>1</sup>  
CONSTANTIN BAUER,<sup>3</sup> ANDREA STADLER,<sup>1</sup> FABIAN BUCHFELLNER,<sup>1</sup>  
ROLF KUTTLER,<sup>1</sup> MARTIN JAKOBI,<sup>2</sup> WOLFRAM VOLK,<sup>3</sup>  
ALEXANDER W. KOCH,<sup>2</sup> AND JOHANNES ROTHS<sup>1</sup>

<sup>1</sup>Photonics Laboratory, Munich University of Applied Sciences, Munich 80335, Germany

<sup>2</sup>Institute for Measurement Systems and Sensor Technology, Technical University of Munich, Munich 80333, Germany

<sup>3</sup>Chair of Metal Forming and Casting, Technical University of Munich, Garching 85748, Germany

\*qiang.bian@tum.de

**Abstract:** An optical fiber with both temperature and strain fiber Bragg grating sensors were embedded into an aluminum cast structure during the casting process. Temperature and strain calibrations were carried out respectively for the metal-embedded sensors. Temperature and external strain decoupling was further demonstrated in a temperature range from 25 to 80 °C and an external strain range from 0 to ~110  $\mu\epsilon$ . With the interpolated temperature measured by two temperature sensors at different positions, the external strain could be decoupled from temperature and thermal strain at the strain sensor. The temperature and external strain values obtained from our embedded optical fiber sensors agreed well with reference values, revealing the good performance of the metal-embedded optical fiber sensors. The difference between the measured values and the reference values are within  $\pm 5 \mu\epsilon$  for external strain and  $\pm 1$  °C for temperature. With only a single fiber, the in-situ temperature and external strain information in the aluminum structure can be monitored in real time, representing an important step towards fiber-optic smart casts. Our investigation demonstrates that embedded optical fiber sensors can be a promising method for structural health monitoring of metallic structures.

© 2022 Optica Publishing Group under the terms of the [Optica Open Access Publishing Agreement](#)

## 1. Introduction

Optical fiber sensors (OFSs) have the merits of small size, design flexibility, immunity to electromagnetic interference, resistance to corrosion, and the capacity to achieve distributed sensing, which make them becoming a mainstream sensing technology more than just a laboratory exploration. In the recent years, OFSs have been applied in structural health monitoring (SHM) in civil infrastructures [1–3], energy power [4,5], aerospace [6,7], and downhole applications [8].

Compared with those surface-attached sensors and nondestructive methods, embedded sensors can provide in-situ information at some critical locations from inside the structure in real time with a compact sensing system. OFSs embedded in composite structures have been widely investigated in the past ten years [9–12], especially in the field of reinforced laminates [13]. For metallic structures, however, the embedding process is more challenging due to the much higher melting points of metals and the large mismatch of material properties. Laser-based embedding methods, like laser layered manufacturing [14,15] and selective laser melting [16], have been applied in this field. In general, a metallic jacket, nickel, or silver, for instance, needs to be coated onto fibers in advance to act as a conductive layer, but debris and gaps can still be found at the interface after embedding [17]. Besides, correct laser properties must be selected properly to ensure fusing the metal powder without damaging the optical fibers, demanding

significant efforts [15,17]. Another embedding method, called ultrasonic consolidation (UC) [18] or ultrasonic additive manufacturing (UAM) [19], has become a hot topic in recent years. Optical fibers can be bonded with metal foils layer by layer using ultrasonic oscillation [20]. The UC technique can also be combined with laser techniques to modify the surface of metal foils, achieving accurate placement and reduced distortion [21]. The relatively low-temperature requirement is an important feature of this method. However, specific foil thickness, width, and surface roughness are required to achieve valid bonding [22]. The casting process has also been proposed to embed fiber sensors into metals [23]. The challenges of this method include the high melting points of metals, the melt impurity in casting, and the high contraction during the cooling down process. Nonetheless, the advantages of the casting method are obvious. Mass manufacturing is possible with the casting process, and those structures with complex and large shapes needed in the industry, like turbines and engines, can be fabricated. By placing the fiber sensors in advance into the right position of the cast model, these sensors can be easily embedded deep inside metallic structures. Previous research from our group has demonstrated that, with the casting processes, bare optical fibers can be embedded into metals like aluminum [24] and copper [25]. Heilmeier *et al.* carried out tensile tests using aluminum cast specimens with embedded fiber Bragg grating (FBG) strain sensors [26] and evaluated the strain transition properties between fibers and the cast parts by neutron diffraction [27]. Lindner *et al.* investigated the strain and temperature response of fiber embedded cast parts [28].

Decoupling temperature and external strain is another challenge. OFSs like FBGs are normally sensitive to both temperature and strain, so measures should be applied to distinguish these two parameters when fibers are embedded into structures. Some progress has been made in the field of composite structures. Ferreira *et al.* embedded two FBGs into two different composites of the hybrid composite laminates and used the response difference between the composites to decouple temperature and strain [29]. Fazzi *et al.* embedded a tilted FBG (TFBG) into a composite plate and decoupled temperature and strain by tracking the wavelength shifts of the Bragg and the Ghost peaks of TFBG [30]. Marin *et al.* combined FBG and long-period grating (LPG) to monitor the temperature and strain progress during composite materials manufacture, including the curing of epoxy resin and the liquid resin infusion process [31]. Pereira *et al.* achieved independent strain and temperature measurements by embedding two FBGs in a polymeric tensile test specimen with a certain angle between them [32]. However, in metallic structures, according to our knowledge, although some researches studied the temperature and strain behaviors of the embedded OFSs [17] or measured temperature and strain using OFSs, which were not fully surrounded by metals but epoxy glue [33], few researches related to temperature and strain decoupling of OFSs embedded in metallic structures have been reported [34].

In this investigation, we embedded a single optical fiber with three multiplexed FBG sensors into an aluminum cast structure during the casting process. The FBG sensor in the middle was in direct contact with aluminum measuring both temperature and strain, while two FBG sensors at adjacent positions were protected inside capillaries providing temperature information at different positions. Temperature and strain calibration for those embedded OFSs were carried out separately. We solved the cross-sensitivity issue of the middle FBG by using the temperature information provided by the temperature sensors to compensate the influence from temperature and thermal strain, so the external strain information can be obtained. The temperature and external strain values measured from the embedded sensors agreed well with reference values, revealing the good performance of our cast embedded OFSs.

## 2. Principle and structure

### 2.1. Fiber Bragg grating sensors

An FBG is a kind of wavelength-specific reflector inside an optical fiber created by a periodical refractive index modulation inside the fiber's core. The reflected central peak wavelength, also

called Bragg wavelength, is determined by the effective refractive index of the fiber  $n_{eff}$  and the grating period  $\Lambda$  with the relationship  $\lambda_B = 2n_{eff}\Lambda$ . FBGs are inherently sensitive to temperature and strain, and both  $n_{eff}$  and  $\Lambda$  can be influenced by these two parameters, the relationship of which is given by [35]:

$$\Delta\lambda_B(T, \varepsilon) = \Delta\lambda_B(T) + \Delta\lambda_B(\varepsilon), \quad (1)$$

where  $\Delta\lambda_B(T)$  represents the temperature-induced Bragg wavelength variation, and  $\Delta\lambda_B(\varepsilon)$  represents the strain-induced Bragg wavelength variation. For the temperature characteristics of FBGs, it has been found that there is a nonlinear relationship between  $\Delta\lambda_B(T)$  and temperature [36]. The wider the temperature range is, the more obvious the nonlinearity appears. A polynomial function of temperature  $T$  can be used to represent  $\Delta\lambda_B(T)$ . For strain-induced Bragg wavelength variation  $\Delta\lambda_B(\varepsilon)$ , both axial strain  $\varepsilon_z$  and radial strain  $\varepsilon_r$  influence the Bragg wavelength. Therefore, Eq. (1) can be rewritten as [28,37]:

$$\Delta\lambda_B(T, \varepsilon) = \sum_{i=0}^n a_i T^i + \lambda_{B_0} \left\{ \varepsilon_z - \frac{n_{eff}^2}{2} [p_{12}\varepsilon_z + (p_{12} + p_{11})\varepsilon_r] \right\}, \quad (2)$$

where  $p_{11}$  and  $p_{12}$  are Pockels' coefficients,  $a_i$  are polynomial coefficients, and  $\lambda_{B_0}$  is the Bragg wavelength when no strain is present.

Several FBGs with different Bragg wavelengths can be fabricated in a single fiber to achieve multipoint sensing, owing to the multiplexing ability. In this research, by using the phase mask method [38], three type-I FBGs were written in a photosensitive single-mode fiber (GF1B, Nufern, East Granby, USA) with a KrF Excimer laser (MLI-200, MLase AG, Germering, Germany). As shown in Fig. 1(a), the fiber has cladding and core diameters of  $125 \mu\text{m}$  and  $7 \mu\text{m}$ , respectively. The coating of the fiber was removed in advance to avoid burning during the treatment. The length of each FBG was  $3 \text{ mm}$  with a reflectivity of  $\sim 90 \%$ . The distance between each adjacent FBG was  $12 \text{ mm}$ .

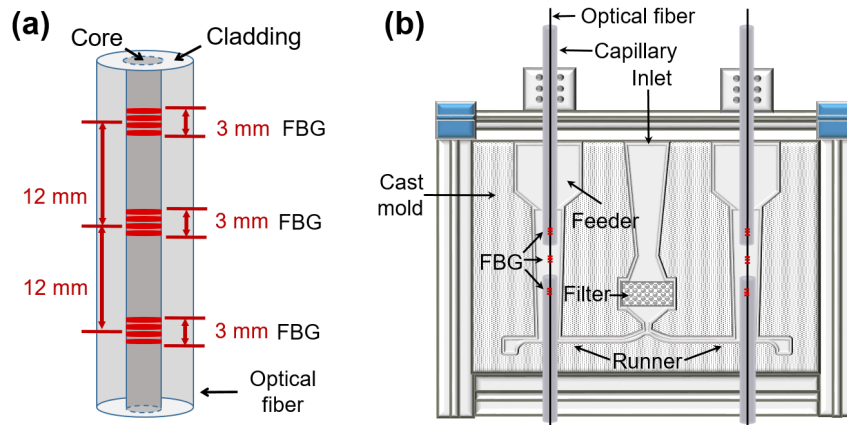


**Fig. 1.** (a) Array of three FBG sensors in a GF1B fiber. (b) Schematic diagram of optical fiber embedding process by casting.

## 2.2. Material and manufacturing

The standardized hypoeutectic alloy AlSi9Cu3 (DIN EN 1706:2010) was used for casting in this research. This alloy is an ideal choice for complex machine and engine parts, owing to the high-temperature strength provided by the high copper concentration, the improved machining properties by the reduced Si concentration, and the high mechanical strength due to the

combination of Si and Cu [39]. Table 1 shows the standardized composition of AlSi9Cu3 and the actual composition of AlSi9Cu3 used in our research, measured by spark emission spectroscopy.

**Table 1. Standardized and actual composition of AlSi9Cu3 alloy.**

Type	Standard [39]	Actual
Al (wt./%)	<i>rem</i>	86.8
Si (wt./%)	8.0 – 11.0	9.1
Mg (wt./%)	0.05 – 0.55	0.21
Fe (wt./%)	0.6 – 1.1	0.74
Cu (wt./%)	2.0 – 4.0	3.1

As shown in Fig. 1(b), a 3D-printed silica sand mold was used to determine the casting shape. Stainless steel capillaries were fixed on the frame and were used to lead the optical fiber to the right position inside the mold. The upper and lower FBGs were protected inside capillaries, while the middle FBG was in direct contact with the aluminum alloy. The molten aluminum alloy (maximum temperature  $\sim 650$  °C) was poured into the mold through the inlet during the casting. In order to improve the casting quality, a filter was used to filter slag from the melt. The molten aluminum flowed through the runners and rose from the lower to the upper position. The feeder was used to provide enough molten aluminum during the solidification process to prevent cavities and voids due to shrinkage. Due to the large difference between thermal expansion coefficients (CTEs) of aluminum and silica, the fiber that was in direct contact with the aluminum alloy suffered from high radial and axial compression during the cooling down process of the casting but still survived.

### 2.3. Specimen structure

After casting, one arm of the aluminum cast part obtained from the abovementioned casting was machined into a tensile test specimen according to [40]. Figure 2(a) and 2(b) show the picture and the schematic diagram of the specimen after machining, respectively. The diameter of the tensile test section was 8 mm, with a uniform region of 40 mm length. The lower section of the specimen was a feeder left in the casting process. The capillary had outer and inner diameters of 0.8 mm and 0.6 mm, respectively. The temperature sensors, called FBG(T)-1 and FBG(T)-2, were protected by the capillaries to keep them away from bending and strain, so they could independently provide temperature information. The strain sensor, called FBG(T,  $\epsilon$ ), was in direct contact with the aluminum alloy and was sensitive to both temperature and strain. The microscope picture of the cross-section, Fig. 2(c), shows that in the region where the fiber was in direct contact with the aluminum alloy, there was no obvious gap or void at the interface, so a good strain transfer from the aluminum to the fiber can be assumed.

### 2.4. Interaction between fiber and aluminum

FBG(T)-1 and FBG(T)-2, collectively called FBG(T)s, were protected by the capillaries, ensuring that there was no strain transferred from the aluminum alloy to the fiber, so the strain-induced Bragg wavelength variation  $\Delta\lambda_B(\epsilon)$  in Eq. (1) can be neglected, and  $\Delta\lambda_B(T)$  is the only valid part for FBG(T)s when the temperature changes.

For FBG(T,  $\epsilon$ ), however, it was located at a position where the fiber was in direct contact with the aluminum alloy. As shown in Fig. 2(c), the fiber was fully surrounded by the aluminum alloy without obvious gap or void, which means both temperature and stress (strain) from surrounding aluminum alloy could influence the FBG(T,  $\epsilon$ ). Even though no external strain was applied, when the temperature changed, the interaction between the fiber and the aluminum alloy brought the thermal strain  $\Delta\lambda_B(\epsilon_{the})$ .

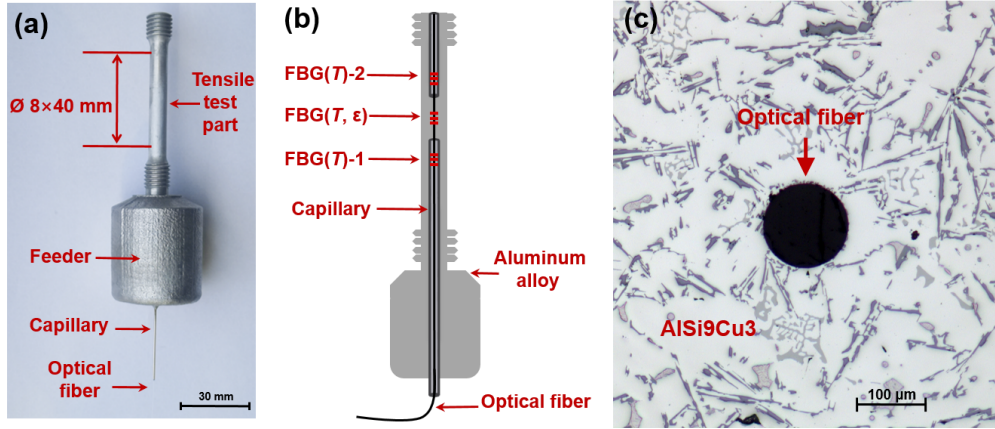


**Fig. 2.** Fiber-embedded aluminum specimen (a) picture, (b) schematic diagram, and (c) microscope picture of the cross-section where the fiber was in direct contact with the aluminum alloy.

To interpret and predict the thermal strain, a shrink-fit model was applied [41–43]. Owing to the parameter mismatch between silica and aluminum, the internal pressure  $p_i$  from the fiber to the surrounding aluminum can be expressed as follows [41,42]:

$$p_i = \frac{(\alpha_{alu} - \alpha_{fiber})E_{alu}E_{fiber}(b^2 - a^2)\Delta T}{\left\{ \begin{array}{l} [(1 + \nu_{alu})E_{fiber} + (1 - \nu_{fiber})E_{alu}]b^2 \\ -[(1 - \nu_{alu})E_{fiber} + (1 - \nu_{fiber})E_{alu}]a^2 \end{array} \right\}}, \quad (3)$$

where  $a$  and  $b$  are the radii of the fiber and the surrounding aluminum alloy,  $\Delta T$  is the temperature difference,  $\alpha_{fiber}$  and  $\alpha_{alu}$  are the CTEs of the fiber and the aluminum alloy,  $E_{fiber}$  and  $E_{alu}$  are the Young's moduli of the fiber and the aluminum alloy,  $\nu_{fiber}$  and  $\nu_{alu}$  are the Poisson's ratios of the fiber and the aluminum alloy, respectively.

Since the radius of fiber is much smaller than that of aluminum alloy ( $a \ll b$ ), a further simplification of the theory can be achieved for the specimen used here. The total radial strain  $\varepsilon_r$  and the total axial strain  $\varepsilon_z$  of the fiber after simplification can be expressed as [28]:

$$\varepsilon_r = \varepsilon_{rr} + \varepsilon_{zr} = \frac{1 - \nu_{fiber}}{E_{fiber}}p_i - \nu_{fiber}(\alpha_{alu} - \alpha_{fiber})\Delta T, \quad (4)$$

$$\varepsilon_z = \varepsilon_{zz} + \varepsilon_{rz} = (\alpha_{alu} - \alpha_{fiber})\Delta T - \frac{2\nu_{fiber}}{E_{fiber}}p_i, \quad (5)$$

where  $\varepsilon_{rr}$  is the pure radial strain,  $\varepsilon_{zr}$  is the transversal effect of the radial strain,  $\varepsilon_{zz}$  is the pure axial strain,  $\varepsilon_{rz}$  is the transversal effect of the axial strain.

Therefore, it can be seen that when the temperature changes, different from  $FBG(T)$ , the Bragg wavelength variation of  $FBG(T, \varepsilon)$  includes two parts:

$$\Delta\lambda'_B(T) = \Delta\lambda_B(T) + \Delta\lambda_B(\varepsilon_{the}), \quad (6)$$

where  $\Delta\lambda_B(T)$  is the pure temperature-induced Bragg wavelength variation, and  $\Delta\lambda_B(\varepsilon_{the})$  is the wavelength variation caused by the thermal strain.

### 3. Experiments and results

The reflective spectrum of the embedded FBG sensors was obtained by connecting the fiber to an FBG interrogator (sm125, MicronOptics, Atlanta, USA). A typical spectrum measured at room temperature without external stress to the aluminum specimen is shown in Fig. 3. Due to the solidification during the casting and cooling process, the fiber suffered from compression and microbendings, so the reflective power of  $\text{FBG}(T, \varepsilon)$  was a bit weaker than that of  $\text{FBG}(T)$ s, which were protected inside the capillaries. For reference purpose, the enlarged spectrum in the inset was obtained with an ASE light source and an optical spectrum analyzer (Advantest Q8384, Anritsu, Tokyo, Japan). The spectrum shows no obvious distortions or multiplexes caused by birefringence or stress gradients in  $\text{FBG}(T, \varepsilon)$ . The spectrum was in good agreement with the spectrum obtained by the sm125, showing the proper operation of the interrogator. A peak-finding algorithm [44] based on fitting a parabolic to the peak of the spectra was applied to measure the Bragg wavelengths of all three FBGs.

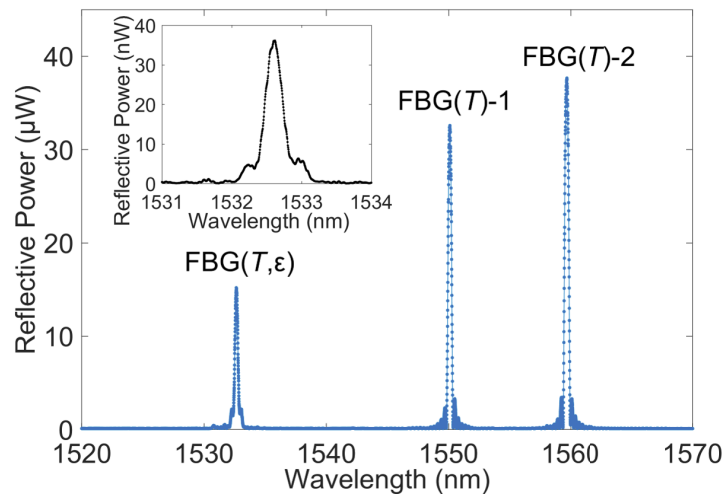


**Fig. 3.** A typical reflective spectrum of the embedded FBG sensors at room temperature, obtained with a sm125 interrogator. For reference the inset shows an enlarged spectrum of  $\text{FBG}(T, \varepsilon)$  obtained with an optical spectrum analyser.

In this section, temperature and strain calibrations were carried out to obtain the temperature sensitivities of  $\text{FBG}(T)$  and  $\text{FBG}(T, \varepsilon)$  and the external strain sensitivity of  $\text{FBG}(T, \varepsilon)$ . After the calibration, a temperature and external strain measurement experiment was carried out to demonstrate the multiparameter sensing capability of the system.

#### 3.1. Temperature calibration

A temperature calibration was carried out to measure the temperature sensitivities of the embedded  $\text{FBG}(T, \varepsilon)$  and  $\text{FBG}(T)$ s when no external stress was applied. As shown in Fig. 4, the aluminum specimen was put into a climatic chamber (VCL 4010, Vötsch, Balingen, Germany), and two temperature cycles were carried out from 0 to 80 °C, with temperature variation of 10 °C and 2 hours duration at each step. The Bragg wavelengths of three FBGs were recorded by the FBG interrogator sm125 with the peak-finding algorithm and then transferred to a PC. A commercial PT100 resistive temperature sensor (JUMO GmbH & Co. KG, Fulda, Germany) was placed beside the specimen as a reference, by which the recorded temperature process was shown in Fig. 5. The recorded Bragg wavelength variations of  $\text{FBG}(T, \varepsilon)$  and  $\text{FBG}(T)$ s at different temperatures (0, 10, 20, 30, 40, 50, 60, 70, 80 °C) in each cycle are shown in Fig. 5(b) and

5(c), respectively. It can be seen that the experimental results show good repeatability from cycle to cycle. According to the shrink-fit model mentioned in Section 2.4 and the parameters in Table 2, the theoretical Bragg wavelength variation of  $FBG(T, \varepsilon)$  at different temperatures can be calculated, as shown as the black dashed line in Fig. 5(b). The theoretical calculations agreed well with the experimental results, proving the availability of the shrink-fit model for our metal-embedded fiber structure.

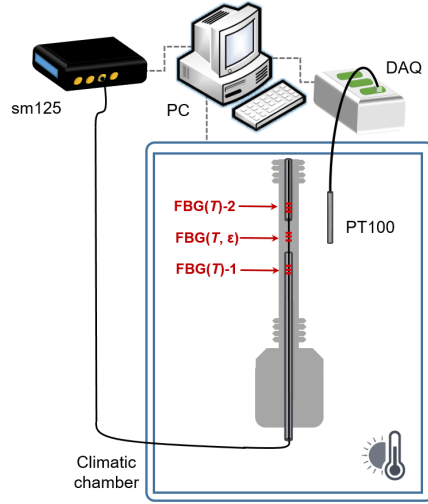


Fig. 4. Schematic diagram of the temperature calibration experiment in a climatic chamber.

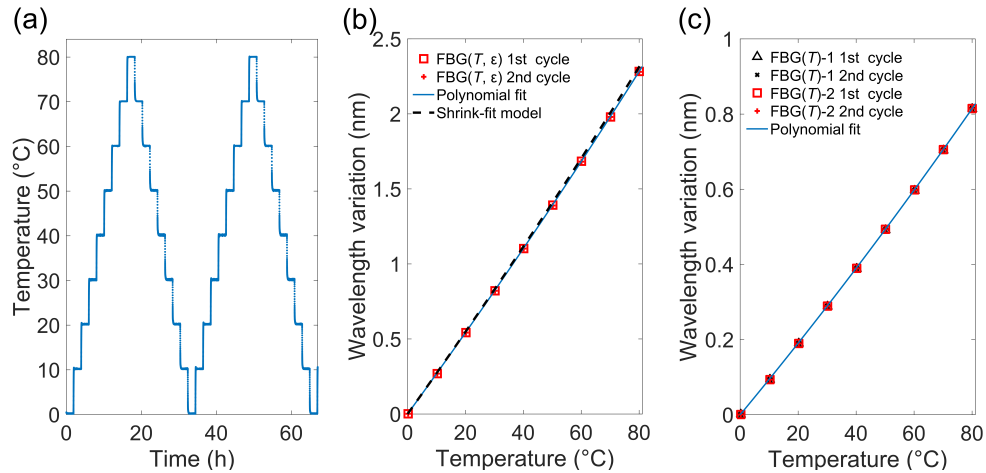


Fig. 5. (a) Temperature process recorded by PT100 temperature sensor. Bragg wavelength variation of (b)  $FBG(T, \varepsilon)$  and (c)  $FBG(T)$ s.

As mentioned in Section 2.1, a polynomial function of temperature  $T$  can be used to represent  $\Delta\lambda_B(T)$ . In our research, to achieve higher precision and better decouple temperature and strain, a second-order calibration polynomial function

$$\Delta\lambda_B(T) = a_1^T T + a_2^T T^2 \quad (7)$$

**Table 2. Parameters of the optical fiber and the aluminum alloy.**

Parameter	Value	Source
$n_{eff}$	1.4473	[45]
$p_{11}$	0.116	[46]
$p_{12}$	0.255	[46]
$E_{fiber}$	74.9 GPa	[47]
$\nu_{fiber}$	0.17	[48]
$\alpha_{fiber}$	$5.5 \times 10^{-7} / ^\circ C$	[48]
$E_{alu}$	75.0 GPa	[49]
$\nu_{alu}$	0.32	[28]
$\alpha_{alu}$	$22.07 \times 10^{-6} / ^\circ C$	[28]
$\frac{d\alpha_{alu}}{dT}$	$0.01794 \times 10^{-6} / ^\circ C$	[28]
$a$	62.5 $\mu m$	[50]
$b$	4 mm	[40]

was used for FBG( $T$ )s according to the polynomial fit method, as shown as the blue solid line in Fig. 5(c). Another second-order calibration was used to represent  $\Delta\lambda'_B(T)$ , which can be expressed as

$$\Delta\lambda'_B(T) = a_1^{T,\varepsilon} T + a_2^{T,\varepsilon} T^2. \quad (8)$$

The fit coefficients of the calibration functions  $a_1^{T,\varepsilon}$  and  $a_2^{T,\varepsilon}$  for FBG( $T, \varepsilon$ ),  $a_1^T$ , and  $a_2^T$  for FBG( $T$ )s, are shown in Table 3.

**Table 3. Coefficients of the second-order polynomial calibration function for FBG sensors.**

Coefficient	$a_1^{T,\varepsilon} (nm/^\circ C)$	$a_2^{T,\varepsilon} (nm/^\circ C^2)$	$a_1^T (nm/^\circ C)$	$a_2^T (nm/^\circ C^2)$
Value	$2.7 \times 10^{-2}$	$2.4 \times 10^{-5}$	$9.3 \times 10^{-3}$	$1.1 \times 10^{-5}$

### 3.2. Strain calibration

A strain calibration at room temperature was carried out to measure the external strain sensitivity of the embedded FBG( $T, \varepsilon$ ), as shown in Fig. 6. The aluminum specimen was fixed into a custom-built tensile test setup, where the external strain was provided by the weights applied to the frame. We assumed that the room temperature was stable during the strain calibration, so the influence from thermal strain was negligible.

Due to the limitation of our custom-built setup, there was a very slight bending in the specimen during the weight loading. Hence, one side was stretched slightly stronger than the other side. We assumed that this bending effect was mainly significant on the surface of the specimen and could be neglected in the interior of the specimen, where the glass fiber was located. Two strain gauges (1-LY13-3/350A, HBM, Darmstadt, Germany) were glued on two opposite surfaces of the test specimen at the longitudinal position where FBG( $T, \varepsilon$ ) was located, so the bending effect can be compensated by [51]:

$$\varepsilon_{ext,exp} = \frac{\varepsilon_{sg,A} + \varepsilon_{sg,B}}{2}, \quad (9)$$

where  $\varepsilon_{ext,exp}$  is the experimentally measured external strain,  $\varepsilon_{sg,A}$  and  $\varepsilon_{sg,B}$  are the strain data obtained from each strain gauge, respectively. During the experiment, the data measured by the strain gauges were collected by a DAQ board (QuantumX MX840B, HBM, Darmstadt, Germany),

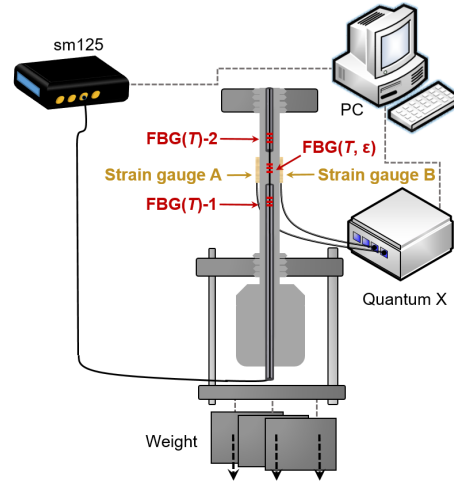


**Fig. 6.** Schematic diagram of the strain calibration experiment in a custom-built tensile test setup.

and the Bragg wavelengths of FBGs were recorded by the interrogator sm125 and then transferred to a PC. An offset weight of 24.76 kg was applied in advance to consolidate the connection between the specimen and the frame, so their relative movement was reduced to a low level. Starting from the offset weight, when the strain was regarded as zero, we increased the loading weight step by step, from 0 kg to 41.6 kg, with 8 steps of 5.2 kg. Three cycles with loading and unloading steps were carried out to check the experimental repeatability, as shown in Fig. 7. According to the theory of linear elasticity, the theoretical external strain can be calculated as follows:

$$\varepsilon_{ext,theo} = \frac{\sigma}{E_{alu}} = \frac{mg}{AE_{alu}} = \frac{mg}{\pi b^2 E_{alu}}, \quad (10)$$

where  $m$  is the loaded weight, and  $A$  is the cross-section area of the specimen. Figure 7(b) shows the theoretically calculated strain  $\varepsilon_{ext,theo}$ , the experimentally measured strain  $\varepsilon_{ext,exp}$  by strain gauges and the corresponding loaded weight. The experimental results agreed well with the theoretical calculations based on Eq. (10) using the parameters in Table 2. This shows that the theoretical calculations were trustable, and each loaded weight could correspond to each external strain.

Then, a strain calibration of the embedded  $FBG(T, \varepsilon)$  was carried out at room temperature. The Bragg wavelength of  $FBG(T, \varepsilon)$  was measured by the interrogator sm125 when the abovementioned three cycles with the same loading and unloading steps were carried out. The Bragg wavelength variation under different external strains was obtained, as shown in Fig. 8.

By averaging the values in each cycle, the external strain sensitivity could be calculated with the linear fit method, as shown as follows:

$$K_{\varepsilon} = \frac{\Delta\lambda_B(\varepsilon_{ext})}{\varepsilon_{ext}} = 1.2847 \text{ pm}/\mu\varepsilon, \quad (11)$$

where  $K_{\varepsilon}$  is the external strain sensitivity of  $FBG(T, \varepsilon)$  embedded in the aluminum cast. As a comparison, the theoretical calculated external strain sensitivity for FBG embedded in aluminum cast parts was reported to be 1.27 pm/ $\mu\varepsilon$  [28], and the strain sensitivity for FBG in a free fiber was measured to be 1.20 pm/ $\mu\varepsilon$  [52].

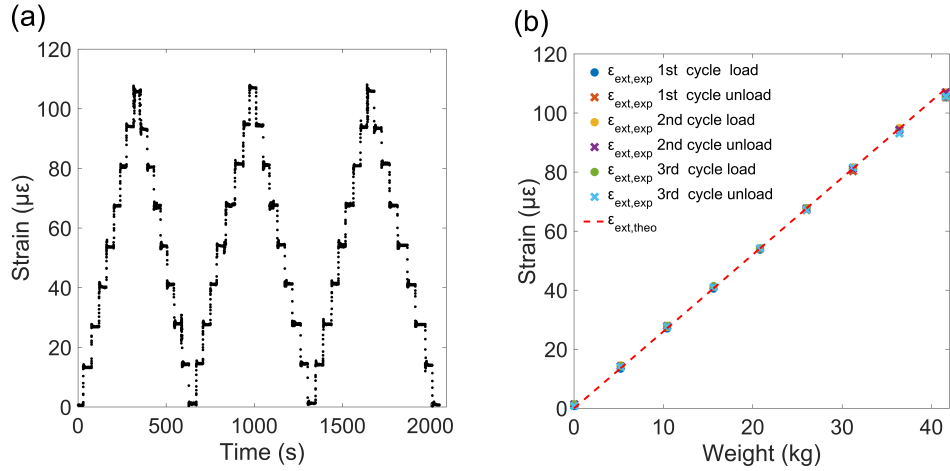


**Fig. 7.** (a) Experimentally measured external strain  $\epsilon_{ext,exp}$  by strain gauges in strain calibration process with three cycles. (b) Loaded weight and corresponding experimental/theoretical external strain.

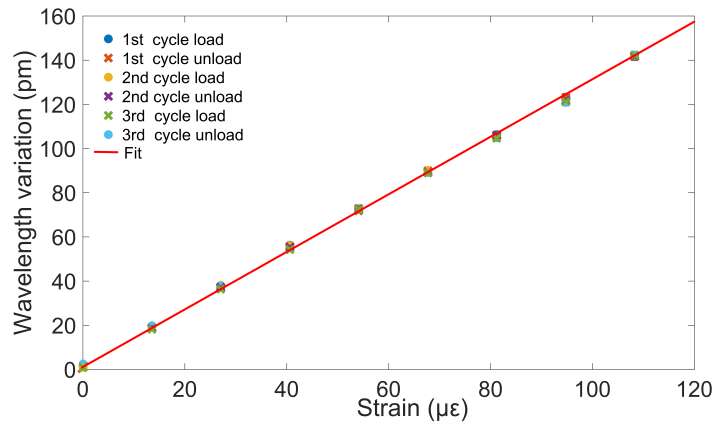


**Fig. 8.** Bragg wavelength variation of  $FBG(T, \epsilon)$  under different strains at room temperature.

### 3.3. Temperature and external strain measurement

For the embedded fiber sensors, the temperature and external strain sensitivities were obtained respectively by the temperature and strain calibrations described above. For  $\text{FBG}(T, \varepsilon)$ , the Bragg wavelength was influenced both by temperature and external strain, as shown as follows:

$$\lambda_B(T, \varepsilon) = \lambda_0 + \Delta\lambda'_B(T) + \Delta\lambda_B(\varepsilon_{ext}), \quad (12)$$

where  $\lambda_0$  is the Bragg wavelength at  $0^\circ\text{C}$  and  $0 \mu\varepsilon$ , which has been measured in advance. We assumed that the external strain sensitivity was independent of temperature for the limited temperature range and Eq. (11) was valid in the temperature range applied. Therefore, by substituting Eq. (8) and Eq. (11) into Eq. (12), the external strain can be decoupled from the temperature in  $\text{FBG}(T, \varepsilon)$ , as shown as follows:

$$\varepsilon_{ext} = \frac{\lambda_B(T, \varepsilon) - \lambda_0 - a_1^{T,\varepsilon}T - a_2^{T,\varepsilon}T^2}{K_\varepsilon}. \quad (13)$$

Here,  $T$  is the temperature at the location of  $\text{FBG}(T, \varepsilon)$ , which can be predicted with the temperatures measured by  $\text{FBG}(T)$ -1 and  $\text{FBG}(T)$ -2 according to an interpolation method:

$$T = \frac{T_{temp1} + T_{temp2}}{2}, \quad (14)$$

where  $T_{temp1}$  and  $T_{temp2}$  are the temperatures measured by  $\text{FBG}(T)$ -1 and  $\text{FBG}(T)$ -2, respectively.

A temperature and strain measurement experiment was carried out to check the temperature and external strain sensing ability. The schematic diagram of the setup used is shown in Fig. 9. This setup was similar to that in the strain calibration experiment, but the strain gauges were removed and replaced by heating foils surrounding the cylindrical and feeder parts of the specimen. With the NTC sensor, the connected PID controller, and the heating foils, the temperature of the specimen was controlled to be stabilized at temperatures of  $25^\circ\text{C}$ ,  $30^\circ\text{C}$ ,  $40^\circ\text{C}$ ,  $50^\circ\text{C}$ ,  $60^\circ\text{C}$ ,  $70^\circ\text{C}$ , and  $80^\circ\text{C}$ . Extra insulation foam was used to cover the heating region to improve the temperature homogeneity and stability.

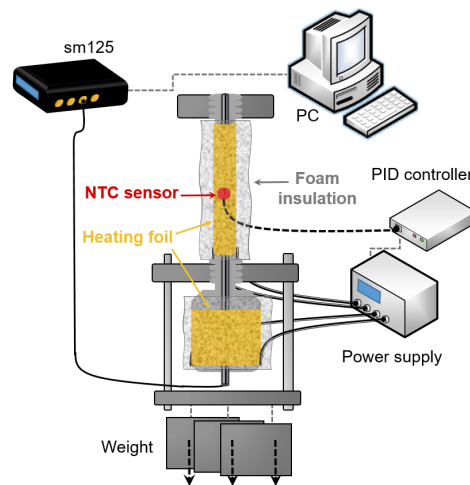


**Fig. 9.** Schematic diagram of the temperature and strain measurement experiment.

At each controlled temperature level, loading and unloading steps mentioned in Section 3.2 were performed. As an example, Fig. 10 (a), (b), and (c) show the Bragg wavelength variations

of  $\text{FBG}(T, \varepsilon)$ ,  $\text{FBG}(T)$ -1, and  $\text{FBG}(T)$ -2 during three strain cycles at a temperature of  $80^\circ\text{C}$ , respectively. As seen in Fig. 10(a), the Bragg wavelength of  $\text{FBG}(T, \varepsilon)$  changed as time owing to the loading and unloading steps, while, in Fig. 10(b) and 10(c), the Bragg wavelengths of  $\text{FBG}(T)$ -1 and  $\text{FBG}(T)$ -2 remained constant, revealing that  $\text{FBG}(T)$ s were independent to strain and the temperature environment provided by the heating foils was stable.

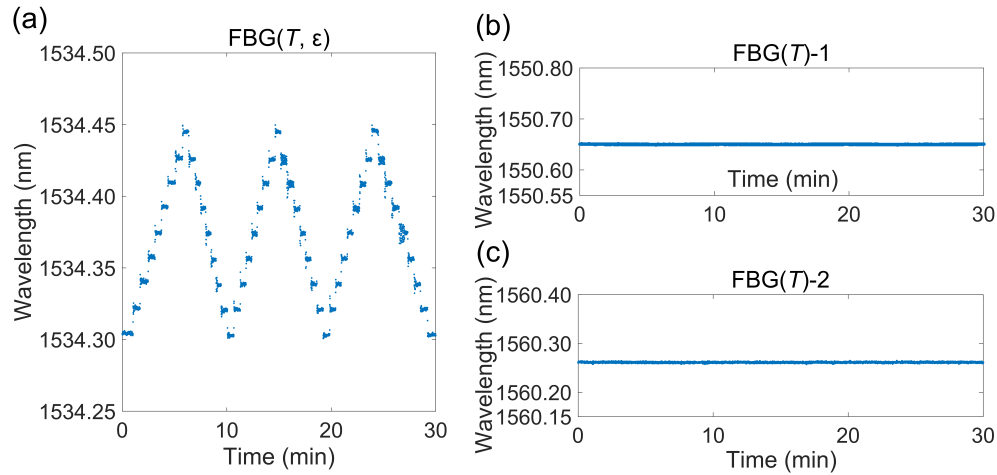


**Fig. 10.** Bragg wavelength variation of (a)  $\text{FBG}(T, \varepsilon)$ , (b)  $\text{FBG}(T)$ -1, (c)  $\text{FBG}(T)$ -2 during the strain cycles at  $80^\circ\text{C}$ .

The temperature values were calculated based on Eq. (14), and the external strain values were decoupled from the temperature and thermal strain in  $\text{FBG}(T, \varepsilon)$  according to Eq. (13). The reference temperature was from the NTC sensor, while the reference strain was based on the theoretical calculations according to Eq. (10), respectively. Figure 11(a) shows the strain obtained by FBG sensors and by reference at different temperatures, while Fig. 11(b) shows the FBG measured temperature and reference temperature at different strains. The error bars for each measurement was also plotted in each figure. The black line represents the linear function when FBG measured value is equal to the reference value. To better show the decoupled temperature and strain at the same time, we plot Fig. 11(c), where the red cross symbols represent the measured values from FBG sensors and black circle symbols represent the reference values. The results show that the temperature and strain values obtained from the embedded FBG sensors agreed well with reference values, revealing the good multiparameter sensing capability of our cast embedded OFSs. The difference between measured values and reference values are within  $\pm 5 \mu\varepsilon$  for external strain and  $\pm 1^\circ\text{C}$  for temperature.

The main reason of the difference between measured values and reference values might come from the limitation of the heating foil because it has been found that there was a slight temperature difference between the surface and the interior of the specimen. According to the decoupling method in Eq. (13), this temperature difference would lead to a strain deviation, especially in this case where the temperature sensitivity of  $\text{FBG}(T, \varepsilon)$  was much higher than its external strain sensitivity. Besides, our custom-built setup can only provide the external strains up to  $110 \mu\varepsilon$ , while in the real applications, typical tensile strains can be one or two orders of magnitude higher, in which scenario the strain difference ( $\pm 5 \mu\varepsilon$ ) would be small enough. Therefore, we believe that our metal-embedded OFSs show a good performance in providing temperature and external strain information.

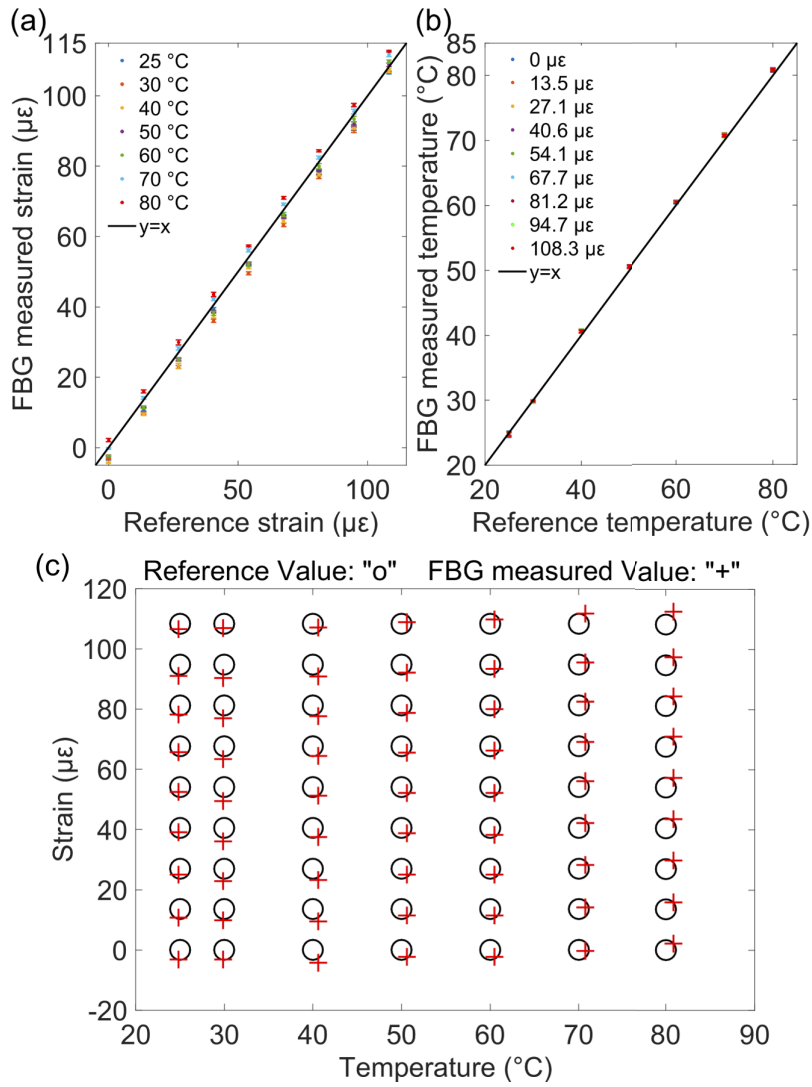


**Fig. 11.** (a) Strain measured by FBG sensors and by reference at different temperatures. (b) Temperature measured by FBG sensors and by reference at different strains. (c) Reference value (circle) and measured value (cross) obtained from FBG sensors at different temperatures and strains.

#### 4. Conclusion

An optical fiber with both temperature and strain FBG sensors was embedded into an aluminum cast structure during the casting process. The strain sensor  $\text{FBG}(T, \varepsilon)$  was in direct contact with aluminum, while the adjacent placed temperature sensors  $\text{FBG}(T)$ s were protected from strains by capillaries. A temperature calibration in a climatic chamber from 0 to 80 °C and a strain calibration in a custom-built tensile test setup from 0 to  $\sim 110 \mu\varepsilon$  at room temperature were carried out respectively for the embedded sensors. A shrink-fit model was applied to analyze the interaction between the aluminum and the embedded fiber and predict the thermal strain at different temperatures. The theoretical calculations and the experimental results in the temperature calibration experiment matched well, showing the validity of the shrink-fit model for our structure. The cross-sensitivity issue was well solved: external strain can be decoupled from the temperature and thermal strain in the strain sensor using the interpolated temperature information provided by the temperature sensors. The temperature and strain values obtained from our embedded sensors agreed well with reference values.

Our investigation demonstrated that embedded OFSs could be a promising method for in-situ SHM of metallic cast structures. Temperature and external strain can be measured inside a cast part with a single sensing fiber, representing an important step towards fiber-optic smart casts. More sensing points with tens of FBGs can be achieved due to the multiplexing ability, which allows extending the SHM capability of the fiber-optic system to complex metallic structures. Besides, during the casting manufacturing process itself, the optical sensors can be embedded deep inside the metallic structures, and no additional additive manufacturing process is needed, which shows potential for mass manufacturing. Further research could be carried out to extend the measured range of temperature and strain, which would expand the application scenarios. With embedded OFSs, SHM of other metallic materials such as copper and steel, and other physical parameters such as humidity and vibration, could also be further investigated.

**Funding.** Deutsche Forschungsgemeinschaft (KO 2111/11-2, RO 4145/3-2, VO 1487/11-2); China Scholarship Council (201903170207).

**Disclosures.** The authors declare no conflicts of interest.

**Data availability.** Data underlying the results presented in this paper are not publicly available at this time but may be obtained from the authors upon reasonable request.

#### References

1. H. Wang, P. Xiang, and L. Jiang, "Optical fiber sensor based in-field structural performance monitoring of multilayered asphalt pavement," *J. Lightwave Technol.* **36**(17), 3624–3632 (2018).
2. H. Woschitz, F. Klug, and W. Lienhart, "Design and calibration of a fiber-optic monitoring system for the determination of segment joint movements inside a hydro power dam," *J. Lightwave Technol.* **33**(12), 2652–2657 (2014).
3. C. Hu, Z. Yu, and A. Wang, "An all fiber-optic multi-parameter structure health monitoring system," *Opt. Express* **24**(18), 20287–20296 (2016).
4. Z. Fan, X. Diao, M. Liu, Y. Zhang, Z. Huang, and H. Yan, "On-line monitoring of sealing glass in electrical penetration assembly based on femto-laser inscribed fiber bragg grating sensors," *Opt. Express* **27**(2), 608–620 (2019).
5. L. Albero Blanquer, F. Marchini, J. R. Seitz, N. Daher, F. Bétermier, J. Huang, C. Gervillié, and J.-M. Tarascon, "Optical sensors for operando stress monitoring in lithium-based batteries containing solid-state or liquid electrolytes," *Nat. Commun.* **13**(1), 1153 (2022).
6. M. Nicolas, R. Sullivan, and W. Richards, "Large scale applications using FBG sensors: determination of in-flight loads and shape of a composite aircraft wing," *Aerospace* **3**(3), 18 (2016).
7. F. Dutz, S. Boje, U. Orth, A. Koch, and J. Roths, "High-temperature profile monitoring in gas turbine exhaust-gas diffusors with six-point fiber-optic sensor array," *Int. J. Turbomach. Propuls. Power* **5**(4), 25 (2020).
8. Y.-T. Ho, Y.-L. Wang, L.-C. Chang, T.-P. Wang, and J.-P. Tsai, "Optical system for monitoring groundwater pressure and temperature using fiber bragg gratings," *Opt. Express* **29**(11), 16032–16045 (2021).
9. B. De Pauw, S. Goossens, T. Geernaert, D. Habas, H. Thienpont, and F. Berghmans, "Fibre Bragg gratings in embedded microstructured optical fibres allow distinguishing between symmetric and anti-symmetric lamb waves in carbon fibre reinforced composites," *Sensors* **17**(9), 1948 (2017).
10. M. Yeager, M. Todd, W. Gregory, and C. Key, "Assessment of embedded fiber Bragg gratings for structural health monitoring of composites," *Struct. Health Monit.* **16**(3), 262–275 (2017).

11. C. Keulen, B. Rocha, M. Yildiz, and A. Suleman, "Embedded fiber optic sensors for monitoring processing, quality and structural health of resin transfer molded components," *J. Phys.: Conf. Ser.* **305**, 012135 (2011).
12. F. Valvona, J. Toti, V. Gattulli, and F. Potenza, "Effective seismic strengthening and monitoring of a masonry vault by using glass fiber reinforced cementitious matrix with embedded fiber Bragg grating sensors," *Composites, Part B* **113**, 355–370 (2017).
13. R. Prussak, D. Stefaniak, E. Kappel, C. Hühne, and M. Sinapius, "Smart cure cycles for fiber metal laminates using embedded fiber Bragg grating sensors," *Compos. Struct.* **213**, 252–260 (2019).
14. X. Li and F. Prinz, "Metal embedded fiber Bragg grating sensors in layered manufacturing," *J. Manuf. Sci. Eng.* **125**(3), 577–585 (2003).
15. H. Alemohammad and E. Toyserkani, "Metal embedded optical fiber sensors: Laser-based layered manufacturing procedures," *J. Manuf. Sci. Eng.* **133**(3), 031015 (2011).
16. D. Havermann, J. Mathew, W. MacPherson, D. Hand, and R. Maier, "Measuring residual stresses in metallic components manufactured with fibre Bragg gratings embedded by selective laser melting," in *24th International Conference on Optical Fibre Sensors*, vol. 9634 (International Society for Optics and Photonics, 2015), p. 96340T.
17. D. Havermann, J. Mathew, W. MacPherson, R. Maier, and D. Hand, "Temperature and strain measurements with fiber Bragg gratings embedded in stainless steel 316," *J. Lightwave Technol.* **33**(12), 2474–2479 (2014).
18. D. Li and R. Soar, "Plastic flow and work hardening of Al alloy matrices during ultrasonic consolidation fibre embedding process," *Mater. Sci. Eng., A* **498**(1–2), 421–429 (2008).
19. X. He, Z. Wang, D. Wang, X. Wang, Y. Liu, F. Jiang, and L. Yuan, "Optical fiber sensor for strain monitoring of metallic device produced by very high-power ultrasonic additive manufacturing," *IEEE Sens. J.* **19**(22), 10680–10685 (2019).
20. D. White, "Ultrasonic object consolidation," (2003). US Patent 6, 519, 500.
21. S. Masurtschak, R. Friel, A. Gillner, J. Ryll, and R. Harris, "Fiber laser induced surface modification/manipulation of an ultrasonically consolidated metal matrix," *J. Mater. Process. Technol.* **213**(10), 1792–1800 (2013).
22. N. Saheb and S. Mekid, "Fiber-embedded metallic materials: From sensing towards nervous behavior," *Materials* **8**(11), 7938–7961 (2015).
23. C. Lee, J. Alcoz, W. Gibler, R. Atkins, and H. Taylor, "Method for embedding optical fibers and optical fiber sensors in metal parts and structures," in *Fiber Optic Smart Structures and Skins IV*, vol. 1588 (International Society for Optics and Photonics, 1991), pp. 110–116.
24. K. Weraneck, F. Heilmeier, M. Lindner, M. Graf, M. Jakobi, W. Volk, J. Roths, and A. Koch, "Strain measurement in aluminium alloy during the solidification process using embedded fibre Bragg gratings," *Sensors* **16**(11), 1853 (2016).
25. Q. Bian, C. Bauer, A. Stadler, M. Lindner, M. Jakobi, W. Volk, A. Koch, and J. Roths, "In-situ high temperature and large strain monitoring during a copper casting process based on regenerated fiber Bragg grating sensors," *J. Lightwave Technol.* **39**(20), 6660–6669 (2021).
26. F. Heilmeier, R. Koos, K. Weraneck, M. Lindner, M. Jakobi, J. Roths, A. Koch, and W. Volk, "In-situ strain measurements in the plastic deformation regime inside casted parts using fibre-optical strain sensors," *Prod. Eng.* **13**(3–4), 351–360 (2019).
27. F. Heilmeier, R. Koos, M. Singer, C. Bauer, P. Hornberger, J. Hiller, and W. Volk, "Evaluation of strain transition properties between cast-In fibre Bragg gratings and cast aluminium during uniaxial straining," *Sensors* **20**(21), 6276 (2020).
28. M. Lindner, A. Stadler, G. Hamann, B. Fischer, M. Jakobi, F. Heilmeier, C. Bauer, W. Volk, A. Koch, and J. Roths, "Fiber Bragg sensors embedded in cast aluminum parts: axial strain and temperature response," *Sensors* **21**(5), 1680 (2021).
29. M. S. Ferreira, J. Vieira, C. Frias, and O. Fraz ao, "Simultaneous measurement of strain and temperature using fiber Bragg grating sensors embedded in hybrid composite laminates," *Meas. Sci. Technol.* **22**(4), 045206 (2011).
30. L. Fazzi, S. Valvano, A. Alaimo, and R. Groves, "A simultaneous dual-parameter optical fibre single sensor embedded in a glass fibre/epoxy composite," *Compos. Struct.* **270**, 114087 (2021).
31. E. Marin and Y. Ouerdane, "Dual-fibre Bragg grating sensor for simultaneous temperature and strain sensing of composite materials manufacturing," in *EWSHM-7th European Workshop on Structural Health Monitoring*, (2014).
32. G. Pereira, M. McGugan, and L. Mikkelsen, "Method for independent strain and temperature measurement in polymeric tensile test specimen using embedded FBG sensors," *Polym. Test.* **50**, 125–134 (2016).
33. S. Triollet, L. Robert, E. Marin, and Y. Ouerdane, "Discriminated measures of strain and temperature in metallic specimen with embedded superimposed long and short fibre Bragg gratings," *Meas. Sci. Technol.* **22**(1), 015202 (2010).
34. A. Stadler, M. Lindner, Q. Bian, G. Hamann, C. Bauer, W. Volk, M. Jakobi, A. Koch, and J. Roths, "Decoupled temperature and strain measurement with regenerated fiber bragg gratings during an aluminum casting process," in *Sensors and Smart Structures Technologies for Civil, Mechanical, and Aerospace Systems 2021*, vol. 11591 (International Society for Optics and Photonics, 2021), p. 115912D.
35. Y. Liao and M. Li, in *Fiber optics*, (Beijing, Tsinghua University Press, 2000), pp. 198–204,
36. M. Lindner, E. Tunc, K. Weraneck, F. Heilmeier, W. Volk, M. Jakobi, A. Koch, and J. Roths, "Regenerated Bragg grating sensor array for temperature measurements during an aluminum casting process," *IEEE Sens. J.* **18**(13), 5352–5360 (2018).

37. K. Hill and G. Meltz, "Fiber Bragg grating technology fundamentals and overview," *J. Lightwave Technol.* **15**(8), 1263–1276 (1997).
38. K. Hill, B. Malo, F. Bilodeau, D. Johnson, and J. Albert, "Bragg gratings fabricated in monomode photosensitive optical fiber by UV exposure through a phase mask," *Appl. Phys. Lett.* **62**(10), 1035–1037 (1993).
39. "Aluminium and aluminium alloys-castings—chemical composition and mechanical properties," Standard, International Organization for Standardization (2007).
40. "Testing of metallic materials - Tensile test pieces," Standard, DIN-Normenausschuss Materialprüfung (2016).
41. Y. Li, Z. Hua, F. Yan, and P. Gang, "Metal coating of fiber Bragg grating and the temperature sensing character after metallization," *Opt. Fiber Technol.* **15**(4), 391–397 (2009).
42. Y. Feng, "Study on sensing performance of fiber Bragg grating embedded in metal structures," Ph.D. thesis, Nanchang University (2009).
43. J. He, L. Ding, J. Cai, W. Zhu, and J. Dai, "A novel high temperature resistant Mo-Cu functional gradient coating for optic fiber Bragg grating," *Results Phys.* **14**, 102456 (2019).
44. T. Bodendorfer, M. Muller, F. Hirth, and A. Koch, "Comparison of different peak detection algorithms with regards to spectrometric fiber Bragg grating interrogation systems," in *2009 International Symposium on Optomechatronic Technologies*, (2009), pp. 122–126.
45. F. Juelich and J. Roths, "OP2-determination of the effective refractive index of various single mode fibres for fibre Bragg grating sensor applications, Proc. OPTO 2009 & IRS<sup>2</sup> 2009 pp. 119–124 (2009).
46. X. Roselló-Mechó, M. Delgado-Pinar, A. Díez, and M. Andrés, "Measurement of Pockels' coefficients and demonstration of the anisotropy of the elasto-optic effect in optical fibers under axial strain," *Opt. Lett.* **41**(13), 2934–2937 (2016).
47. M. Lindner, D. Bernard, F. Heilmeyer, M. Jakobi, W. Volk, A. Koch, and J. Roths, "Transition from purely elastic to viscoelastic behavior of silica optical fibers at high temperatures characterized using regenerated Bragg gratings," *Opt. Express* **28**(5), 7323–7340 (2020).
48. A. Othonos, "Fiber Bragg gratings," *Rev. Sci. Instrum.* **68**(12), 4309–4341 (1997).
49. Z. D. GmbH, "Eigenschaften von Gussstücken aus Aluminiumlegierungen bei 20°C," <https://www.zismann.de/images/zismann/Eigenschaften226D.pdf>.
50. Coherent, Inc., "Photosensitive Single-Mode Fibers," [https://content.coherent.com/pdf/gf1b\\_spec\\_202011122119.pdf](https://content.coherent.com/pdf/gf1b_spec_202011122119.pdf) (2020).
51. H. B. M. GmbH, "Applying the Wheatstone Bridge Circuit - Technical Information," <https://www.hbm.com/en/7163/wheatstone-bridge-circuit/>.
52. J. Roths and F. Jülich, "Determination of strain sensitivity of free fiber Bragg gratings," in *Optical Sensors 2008*, vol. 7003 (International Society for Optics and Photonics, 2008), p. 700308,